

538,316

Rec'd PCT/PTO 13 JUN 2006

(12) INTERNATIONAL APPLICATION PUBLISHED UNDER THE PATENT COOPERATION TREATY (PCT)

(19) World Intellectual Property  
Organization  
International Bureau



10/538316



(43) International Publication Date  
8 July 2004 (08.07.2004)

PCT

(10) International Publication Number  
WO 2004/057375 A1

(51) International Patent Classification<sup>7</sup>: G01V 11/00

(21) International Application Number:  
PCT/GB2003/005395

(22) International Filing Date:  
11 December 2003 (11.12.2003)

(25) Filing Language: English

(26) Publication Language: English

(30) Priority Data:  
0229991.5 21 December 2002 (21.12.2002) GB

(71) Applicants (for all designated States except US):  
SCHLUMBERGER HOLDINGS LIMITED [—/—];  
P.O. Box 71, Craigmuir Chambers, Road Town, Tor-  
tola (VG). SCHLUMBERGER CANADA LIMITED  
[CA/CA]; 525 - 3rd Avenue S.W., Calgary, Alberta T2P

0G4 (CA). SERVICES PETROLIERS SCHLUM-  
BERGER [FR/FR]; 42, rue Saint Dominique, F-75007  
Paris (FR).

(72) Inventors; and

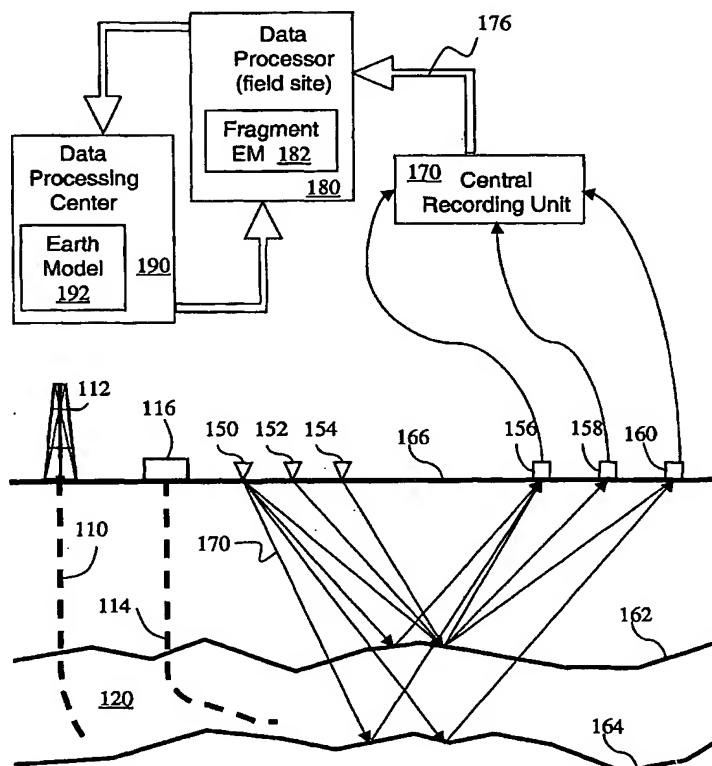
(75) Inventors/Applicants (for US only): ASSA, Steven,  
Brent [US/GB]; 8, The Crescent, Storeys Way, Cambridge  
CB3 0AZ (GB). RAMSHORN, Christoph [DE/GB]; 32  
Humberstone Road, Cambridge CB4 1JF (GB).

(74) Agent: MIRZA, Akram, Karim; Intellectual Property  
Law Department, Schlumberger Cambridge Research Lim-  
ited, High Cross, Madingley Road, Cambridge CB3 0EL  
(GB).

(81) Designated States (national): AE, AG, AL, AM, AT, AU,  
AZ, BA, BB, BG, BR, BY, BZ, CA, CH, CN, CO, CR, CU,  
CZ, DE, DK, DM, DZ, EC, EE, ES, FI, GB, GD, GE, GH,  
GM, HR, HU, ID, IL, IN, IS, JP, KE, KG, KP, KR, KZ, LC,  
LK, LR, LS, LT, LU, LV, MA, MD, MG, MK, MN, MW,  
MX, MZ, NI, NO, NZ, OM, PG, PH, PL, PT, RO, RU, SC,

[Continued on next page]

(54) Title: SYSTEM AND METHOD FOR REPRESENTING AND PROCESSING AND MODELING SUBTERRANEAN SUR-  
FACES





SD, SE, SG, SK, SL, SY, TJ, TM, TN, TR, TT, TZ, UA,  
UG, US, UZ, VC, VN, YU, ZA, ZM, ZW.

(84) Designated States (regional): ARIPO patent (BW, GH, GM, KE, LS, MW, MZ, SD, SL, SZ, TZ, UG, ZM, ZW), Eurasian patent (AM, AZ, BY, KG, KZ, MD, RU, TJ, TM), European patent (AT, BE, BG, CH, CY, CZ, DE, DK, EE, ES, FI, FR, GB, GR, HU, IE, IT, LU, MC, NL, PT, RO, SE, SI, SK, TR), OAPI patent (BF, BJ, CF, CG, CI, CM, GA, GN, GQ, GW, ML, MR, NE, SN, TD, TG).

**Published:**

- with international search report
- before the expiration of the time limit for amending the claims and to be republished in the event of receipt of amendments

*For two-letter codes and other abbreviations, refer to the "Guidance Notes on Codes and Abbreviations" appearing at the beginning of each regular issue of the PCT Gazette.*

System and Method for Representing and Processing and  
Modeling Subterranean Surfaces

FIELD OF THE INVENTION:

5       The present invention relates to the field of earth  
models for subterranean surfaces. In particular, the  
invention relates to systems and methods for improved  
representations and processing techniques for  
subterranean earth surfaces in earth models used in the  
10   exploration and production of hydrocarbon reservoirs.

BACKGROUND OF THE INVENTION:

      In the field of processing earth model data for use  
in the extraction of hydrocarbons from the earth,  
15   significant resources have been invested in creating  
functionality and stabilizing the software quality of  
modeling technology. The efforts have been based on  
faceted representations, and in particular triangulated  
surface methods. However, there are number of key  
20   problems associated with extending triangulated surface  
methods.

      1.   Sampling a smooth surface discretely, for  
example with points arranged in a triangle mesh, is  
inherently inefficient. In contrast, smooth surfaces can  
25   be represented as a Taylor series or as an eigen-function  
expansion, e.g., Fourier series of some form. An eigen-  
function expansion can be used to compute an algebraic  
expression to evaluate normal fields, tangent fields,  
etc. This is inherently more compact and efficient than a  
30   2D or 3D sampling lattice with some sort of  
interpolation.

2. The lack of differentiation makes calculation of a triangulated surface intersection algorithm numerically delicate.

3. Triangles can be used to define shape, but triangles do not efficiently convey an intuitive sense of shape. High resolution and high sampling density make the problem more difficult.

4. Low efficiency triangulation forces application developers to either worry about memory management or to curb flexibility of data set processing.

5. Efficient management of large models means localizing change. It is possible in principle to develop localization methods using triangulated surface models but there are numerical stability issues seen in reference to intersection.

#### SUMMARY OF THE INVENTION:

Thus, it is an object of the present invention to provide an improved system and method for processing data used for hydrocarbon extraction.

Advantageously the invention allows for improved memory and CPU efficiency of implicit surface construction and editing algorithms.

According to the invention a method is provided for processing data used for hydrocarbon extraction from the earth. The method includes the following steps. Receiving sampled data representing earth structures. Identifying one more symmetry transformation groups from the sampled data. Identifying a set of critical points from the sampled data. Generating a plurality of subdivisions of shapes, the subdivisions together representing the earth structures, the generation being based at least in part on the set of identified critical

points and the symmetry transformation groups. Processing  
earth model data using the generated subdivision of  
shapes. And, altering activity relating to extraction of  
hydrocarbons from a hydrocarbon reservoir based on the  
5 processed earth model data.

The identified symmetry transformation group is  
preferably a set of diffeomorphisms that act on a  
topologically closed and bounded region in space-time  
such that under transformation the region occupies the  
10 same points in space.

The identified symmetry transformation groups  
preferably correspond to a plurality of shape families,  
each of which includes a set of predicted critical  
points. The subdivisions are preferably generated such  
15 that a shape family is selected from the plurality of  
shape families that corresponds to the identified  
symmetry transformation group. The selection is  
preferably being based on closeness of correspondence  
between the identified critical points from the sampled  
20 data and the predicted critical points of the selected  
shape family.

Each shape family preferably has an associated set  
of symmetry transformation group orbits, with each orbit  
being associated with orbit information that specifies  
25 whether the orbit contains a predicted critical point and  
value of the Gaussian curvature of a point in the orbit.  
The orbit information from the set of symmetry  
transformation group orbits associated with the selected  
shape family is preferably applied to the sampled data  
30 thereby generating a unique specification of a shape from  
the selected shape family. Each of the plurality of  
subdivisions of shapes is preferably generated by

identifying a part of the uniquely specified shape that corresponds to the sampled data. The identified parts are assembled, thereby generating a representation of the earth structures.

5       The plurality of subdivisions are preferably generated such that the number of parameters in each subdivision times the number of subdivisions is substantially less than would be needed using a faceted representation method, and the plurality of subdivisions  
10 is more numerically stable than third order or higher representation.

      The invention is also embodied in a system for improved extraction of hydrocarbons from the earth, and in a computer readable medium capable of causing a  
15 computer system to carry out steps for processing data relating to earth structures for the extraction of hydrocarbons.

#### BRIEF DESCRIPTION OF THE DRAWINGS:

20

Figure 1 shows an open surface and its embedding in a closed surface;

Figure 2 shows a salt mass's steep flanks and overhangs;

25       Figure 3 shows an example of a 4D representation of a field in Turkmanistan;

Figure 4 is an image of the MacKenzie River Delta;

Figure 5 shows some combinations of involved spherical harmonic polynomials, presented in spherical  
30 polar coordinates;

Figure 6 illustrates that in most cases a surface evolves under mcf to a point;

Figures 7a-f forms a series of six images showing  
vpmcf suppressing noise;

Figure 8 illustrates the orthogonality condition of  
the theorem proposed by Athanassenas;

5 Figure 9 is an aerial image of part of Big Bend  
National Park, showing the approximation of a plateau to  
a characteristic length scale cone;

Figure 10 is a side view of a noise cone structure;

10 Figure 11 is a satellite image of the Labrador  
Trough;

Figure 12 shows s a sequence of folded sediment on  
the coast of the Gulf of Oman;

Figure 13 is an image illustrating progressive  
flattening of an overburden covering a large salt  
15 intrusion;

Figure 14 is a diagram illustrating the Morse  
theoretical cell decomposition for a simple configuration  
of a capped and bent cylinder;

20 Figures 15-17 show diagrams to aid in the  
understanding of the bulls eye construction;

Figure 18 shows two views of an example of a monkey  
saddle;

Figure 19a shows the Reeb graph of a standard torus;

25 Figure 19b schematically illustrates a 2D cell  
suspension that is induced from the axes and planes of  
symmetry and critical point theory;

Figure 20 is cross section of the torus shown in  
Figure 19a;

30 Figure 21 is a schematic of the shape synopsis  
diagram of the torus shown in Figure 19a;

Figure 22 is a cyclide that is shaded according to  
Gaussian and mean curvature;

Figure 23a is a bi-torus with its associated REEB diagram;

Figure 23b is the visual representation of the bi-torus shape synopsis diagram;

5        Figure 24 is a diagram of the octree with a coarse level and leaf level shape index relationship indicated;

The Figure 25 is a diagram shows part of the French model;

10       Figure 26 is an image of the topography of Crater Lake, Oregon;

Figure 27 shows a salt weld in the Gulf of Mexico;

Figures 28a-c illustrate an example of the misfit reduction process;

15       Figures 29a-c illustrates an example of blending a non-differentiable join of two collars;

Figure 30 shows as a geological example a water breach as indicated by the white arrow;

Figure 31 is a NASA Shuttle Mission photograph of the Richat Structure in Mauritania;

20       Figure 32 shows the natural analog to a conformal grid with a proportionally spaced correlation scheme;

Figure 33 illustrates a non-conformal 3D Cartesian grid;

25       Figure 34 is an image of the Devil's Potholes, South Africa;

Figure 35 is an image of the Yukon River delta;

Figures 36a and 36b show, for reference, the background Zechstein Salt and the region in the Zechstein where the vsp was acquired;

30       Figure 37 show the frame graph that ties the vsp region of interest to the Zechstein Salt background;



Figures 38a, 38b, 39a and 39b illustrate the separation of faulted sediments from unfaulted sediments;

Figure 40 illustrates a time-lapse seismic evolution;

5     . Figure 41 shows the reference structure for spatial frames to define a topology graph;

Figure 42 is a schematic illustration of the definition of the variables in the mean curvature estimator;

10     Figure 43 is an image of the regularly sampled input surface representing the present example of the top of the salt, rendered by drawing a subset of evenly spaced inlines and crosslines;

Figure 44 shows the surface when re-sampled by interpolating missing sample points;

15     Figure 45 shows the re-sampled surface after 25 iterations of smoothing;

Figure 46 shows the shape index map for the re-sampled surface after 25 iterations of smoothing;

20     Figure 47 shows that there are 33 shapes in the example shown in Figure 46;

Figure 48 is a schematic illustration of a system for improved extraction of hydrocarbons from the earth, according a preferred embodiment of the invention;

25     Figure 49 shows further detail of a data processor according to preferred embodiments of the invention;

Figure 50 shows steps in a method for processing data used for hydrocarbon extraction from the earth, according to preferred embodiments of the invention; and

30     Figure 51 shows further detail of steps in generating an efficient and robust subdivision of shapes, according to preferred embodiments of the invention.

DETAILED DESCRIPTION OF THE INVENTION:

While Low-level curvature-based methods as applied to implicit surfaces are relatively complicated to develop, they do not suffer numerical stability problems. By comparison, on a smooth Riemannian manifold the 3rd derivatives of the square of the signed distance function describes the norm of the 2nd Fundamental Form and the mean curvature. For triangulated surfaces, this result is difficult to apply, because numerical evaluation of 3rd derivatives is not guaranteed to be numerically stable.

According to the invention, differential geometry methods of surface representation will now be described. Many geoscience phenomena are related to some form of fluid flow. If the fluid phenomena under study involve surface tension, then mean curvature flow (mcf) and variants such as volume preserving mean curvature flow (vpmcf) are accurate modeling tools. (For those unfamiliar with mean curvature flow, imagine the fluid front moving normal to each particle of the fluid front.) The behavior of mcf and vpmcf are well understood when either is applied to a smooth convex surface, star-shaped surface, a surface of rotation, or an entire graph.

A reservoir structural framework does not seem to be an ideal input to mcf, because noise levels degrade the accuracy of analytical approximations and framework surfaces in general are not well approximated as convex, star-shaped, etc. This perception is erroneous. Our investigation of curvature-based modeling shows that mcf can be used to semi-automate its own noise suppression. Given smooth surface data, according to the invention a method is provided to decompose that surface into a

connected sum of star-shaped or entire graph or axisymmetric surface patches.

The mathematical foundation of mcf is substantial, so we seek a unified mathematical description of shape and its evolution. The concept of a fibre bundle is satisfactory. Nakahara presents a formal definition of a fibre bundle. Standard examples of fibre bundles are vector fields, e.g., velocity fields, and tensor fields, e.g., stress fields and elastic fields, evaluated over a sub-volume. In classical differential geometry, curvature properties of surfaces are economically studied in a fibre bundle setting. We have found that a 4D fibre bundle representation of a reservoir framework is no more difficult to write down than is a 3D fibre bundle representations. The economy of mathematical representation is attractive now from the research view. It will be attractive from the engineering view, since reuse of concepts limits the amount of technology that must be mastered.

The fibre bundle representation of a surface of revolution has the following parts.

1. A base that is homeomorphic to a loop, e.g., a circle, an ellipse, or a polygonal closed curve.
2. A typical fibre that is homeomorphic to a compact connected part of either a conic section or a polygonal line.
3. A structure-group that is a group of diffeomorphisms that smoothly deforms any instance of the typical fibre to any other instance.

Here are a few shapes that are frequently encountered in earth modeling represented as fibre bundles.

5 a. A torus has a circle base and a circle typical fibre. Its structure group is the rotation group  $SO(3)$ .

10 b. A cyclide is a torus, but the structure group is the rotation group extended by the scale factor diagonal group. Intuitively, it is a skewed torus.

15 c. Any compact planar region  $R$  with a polygonal boundary  $\partial R$  has a natural bundle structure. To see this, compute the region's bounding box  $B$  and embed  $R$  in  $B$ . (Think of  $B$  as a solid.) If there exists a part of  $\partial R$  that does not intersect any of the box faces, then attach a skirt  $S$  of normal rays to  $\partial$ . Then  $S$ ,  $R$ , and  $\partial B$  enclose a sub-volume  $V$ .

20 We have found that  $V$  is the preferred bundle. The base of the bundle is  $\partial R$  and a typical fibre is a polygonal line. The region  $R$  is formed from the rotation of a line segment emanating from the centroid of  $R$  and joined to the boundary  $\partial R$ . The length of the fibre changes instantaneously. The structure group is the  
25 Euclidean group of rigid body transformations. The following diagram summarizes this construction.

30 Figure 1 shows on the left an open surface, i.e. a surface that does not enclose space; on the right, a closed region (the large box) is subdivided by the same surface forming an internal boundary. Figure 2 shows a salt mass's steep flanks and overhangs, it also shows an example of the cyclide shape in depth imaging. This is an

example that challenges existing commercial software. WesternGeco commercial processing used to construct this velocity model has the common limitation of accepting single z-valued ("height field") data only. According to  
5 the invention we describe below a set of planes in the volume of interest such that a multiple z-value body can be subdivided into sections such that each section is single valued with respect to one of the planes. In other words, each plane parameterizes a section of the  
10 reference multi z-valued surface. Each of these planes are equipped with a rotation matrix and translation vector so that the application can orient the surface section so that it appears to be single valued with respect to one of the coordinate planes. (It may be that  
15 the rotated and translated section is normal to the (x,y) coordinate plane, which is frequently unacceptable to grid-based applications.)

Material properties of a volume of earth can change during an evolutionary process. The time scale of the  
20 evolution can vary from wall clock to calendar to geological record. According to the invention, an evolutionary process is represented using a generalization of the fibre bundle method that is employed for shape. This representation is called an  
25 "evolutionary process". Here are its components.

1. The base is a line with period  $\lambda_B$ . A trajectory on the base serves as a clock. The trajectory's sampling increment has units that are  
30 appropriate to wall clock sampling, calendar sampling, or geological record sampling.

2. A trajectory has compact support. This means that the process is defined on a closed at the beginning and open at the end bounded interval of the helicoid.

5 3. Two evolutionary processes  $P_1$  and  $P_2$  can be summed if and only if on a shared interval of the base helicoid  $P_1$  followed by  $P_2$  is identical to  $P_2$  followed by  $P_1$ . The sum of  $P_1$  and  $P_2$  is  $P_1(t)[P_2(t)[v]]$ , where  $t$  is a point in time and  $v$  is  
10 a point in the volume domain of interest.

4. A fibre is a compact path-connected sub-volume. A fibre is associated to each base point. In other words the process time stamps every sub-volume that it affects.

15 5. A structure group is a 1-parameter subgroup of diffeomorphisms that define an evolution, e.g., vpmcf. Since the structure group consists of diffeomorphisms the process must be invertible. In particular, the process cannot induce  
20 singularities in material space. It is preferable to support singularities, so we allow singularities to develop at the end of a process's time interval.

We emphasize that we seek only a geometrical  
25 evolution - not necessarily the true physical evolution - that describes part of the structural framework. In the following example, we recognize uniformly expanding mean curvature flow creates the shape of the individual layers. Each discontinuity in the sediment terminates the  
30 current flow model and is part of the initial conditions that define the new flow. The ensemble of flow problems describes the formation, but a more economical

representation can be defined if we can treat the entire set of restricted flow problems as a single mean curvature flow problem where evolution continues beyond the intermediate singularities. We look for an evolution  
5 of the set of initial conditions for the individual flow problems, given just the oldest sediment as an initial condition.

We describe a sedimentary sequence as a 4D fibre  
10 bundle.

1. The base of the bundle is a finite length piecewise linear curve.

2. A fibre is an infinitesimal layer of  
15 sediment.

3. The bundle's structure group is a set of diffeomorphism groups such that each group defines an instance of uniformly expanding mean curvature flow. Each leg of the bundle base defines a separate  
20 mean curvature flow problem. The transition between mcf problems is exactly matched by the discontinuity in the sediment.

Figure 3 shows an example of a 4D representation of  
25 a field in Turkmanistan. Each layer is a distinct mean curvature flow where the discontinuity is a curvature flow terminator. Working backwards from a flow termination, we see that it is much easier to identify the flow components in the image. Each flow component is  
30 a uniformly expanding set of solutions to mean curvature flow (or volume-preserving mean curvature flow). Ecker shows in his lecture notes that mean curvature flow can evolve cracks and holes in a smooth background. See, K.

Ecker, Lectures on Regularity for Mean Curvature Flow,  
[http://web.mathematik.unifreiburg.de/mi/analysis/lehre/WS0001/Ecker\\_WS0001.ps](http://web.mathematik.unifreiburg.de/mi/analysis/lehre/WS0001/Ecker_WS0001.ps).

Therefore its usefulness is not limited to modeling  
5 smooth elastic behavior.

According to the invention, we show how to construct  
a meandering river as a fibre bundle. Figure 4 is an  
image of the MacKenzie River Delta.

In Figure 4, the river does not intersect itself,  
10 i.e., no oxbow structures are evident. Also, the river  
appears to have constant width. The structure as a fibre  
bundle is clear.

1. The bundle base is a line segment.
- 15 2. The fibre is any convenient approximation  
of the river channel in cross section, e.g., a  
trapezoid.
3. The structure group is the extended  
Euclidean group, which consists of rigid body motion  
20 plus scaling.

At each point along the channel we measure the cross  
section and record its position relative to the image  
coordinate axes whose origin is the lower left corner of  
25 the picture. Given the previous position of the cross  
section, we compute the update to the (x,y) plane  
rotation and translation.

We turn now to the question of recognizing the  
elementary shape basis elements in an implicit surface  
30 representation. Recall that we represent an implicit  
surface as the zero level set of the signed distance  
function (sdf). Our constructor solves the signed



distance function on a 3D structured grid with tri-linear interpolation as a local approximation to sdf.

By definition tri-linear interpolation  $T(x,y,z)$  on a grid cell is

5

$$T(x,y,z) = A_0 + A_1x + A_2y + A_3z + A_4xy + A_5yz + A_6xz + A_7xyz.$$

where the coefficients  $\{A_k\}$  are defined on the grid cell corners.

10

Each term in  $T(x,y,z)$  is an independent 3D spherical harmonic polynomial in Cartesian coordinates. For convenience we enumerate these spherical harmonic polynomials, using the classical  $Y_{mn}$  notation. (See R. Baerheim, Coordinate Free Representation of the

15

Hierarchically Symmetric Tensor of Rank 4 in Determination of Symmetry, Ph.D. thesis, University of Utrecht, #159, 1998, Appendix, pg. 141-143).

$Y(m,n)$	Monomial
$Y(0,0)$	1
$Y(0,1)$	$z$
$\text{Real}(Y(1,1))$	$x$
$\text{Imag}(Y(1,1))$	$y$
$\text{Real}(Y(2,1))$	$xz$
$\text{Imag}(Y(2,1))$	$yz$
$\text{Imag}(Y(2,2))$	$xy$
$\text{Imag}(Y(3,2))$	$xyz$

20

Here are the associated symmetry transformations and the corresponding isomorphism groups involving these spherical harmonic polynomials.

Term	Symmetry generators	Symmetry group
Constant	Constant	$SO(3)$
$X$	$[x] \sim [x]$	$SO(2)$
$Y$	$[y] \sim [y]$	$SO(2)$

Z	$[z] \sim [z]$	SO(2)
X + Y	$[x, y] \sim [y, x]$	Z/2Z
X + Y + XY		
Y + Z	$[y, z] \sim [z, y]$	Z/2Z
Y + Z + YZ		
X + Z	$[x, z] \sim [z, x]$	Z/2Z
X + Z + XZ		
X + Y + Z	$[x, y, z] \sim [y, z, x]$ $[x, y] \sim [y, x]$	Tetrahedron group of order 12
XYZ	$[x, y, z] \sim [y, z, x]$ $[y, z] \sim [-y, -z]$ $[x, y] \sim [y, x]$	Symmetric(4)
XY	$[x, y] \sim [-x, -y]$ $[x, y] \sim [y, x]$	Z/2Z $\oplus$ Z/2Z
YZ	$[y, z] \sim [-y, -z]$ $[y, z] \sim [z, y]$	
XZ	$[x, z] \sim [-x, -z]$ $[x, z] \sim [z, x]$	
XY + XZ	$[x, y, z] \sim [-x, -y, -z]$ $[y, z] \sim [z, y]$	
XZ + YZ	$[x, y, z] \sim [-x, -y, -z]$ $[x, y] \sim [y, x]$	Z/2Z $\oplus$ Z/2Z
XY + YZ	$[x, y, z] \sim [-x, -y, -z]$ $[x, z] \sim [z, x]$	
XY + YZ + ZX	$[x, y, z] \sim [-x, -y, -z]$ $[x, y, z] \sim [y, z, x]$ $[x, y] \sim [y, x]$	Symmetric(4)

Symmetry analysis is a form of spectral analysis applied to the discrete spectrum that is associated with spherical harmonic polynomial expansions. Our estimates of tri-linear interpolation coefficients are noisy, so we need a threshold for dismissing spectral lines.

Figure 5 shows some combinations of involved spherical harmonic polynomials, presented in spherical polar coordinates.

We are interested in conic section fibre bundle shapes. Here is the correspondence of shape to symmetry group.

Symmetry group	Candidate shapes
SO(3)	Sphere
O(2)	Cylinder, spherical torus, elliptical torus, hyperboloid
SO(2)	Cone, paraboloid
Symmetric(4)	Cube
Dihedral(4)	Ellipsoid
Dihedral(3)	Triangular prism
$Z_2 \oplus Z_2$	Rectangular prism
$Z_2$	Cyclide
{1}	Noisy data

5

According to the invention, mean curvature flow and volume-preserving mean curvature flow will now be discussed in further detail. We define a few terms that appear frequently herein. Given a 2D manifold  $M$  and a point  $p \in M$ , let  $\{p_1, p_2\}$  be a local coordinate system for a region containing  $p$  and let  $n$  be an outward pointing normal at  $p$ . Finally the Euclidean inner product of vector  $U_i$  and  $V_j$  is denoted by  $\langle U_i, V_j \rangle$ .

#### Definitions

The First Fundamental Form (1<sup>st</sup> FF) is  $g_{ij} = \left\langle \frac{\partial M}{\partial p^i}, \frac{\partial M}{\partial p^j} \right\rangle$ .

15 The inverse of the 1<sup>st</sup> FF is denoted by  $g^{ij}$ .

The Second Fundamental Form (2<sup>nd</sup> FF) is  $A = [h_{ij}] = - \left\langle \frac{\partial^2 M}{\partial^2 p^i p^j}, n \right\rangle$ .

The Weingarten map is  $W_i^j = g^{jk} h_{ki}$ . (Einstein notation used.)

The eigenvalues of the Weingarten map are the principal curvatures. The trace of the map is the mean curvature, the determinant of the map is the Gaussian curvature. The norm of the 2<sup>nd</sup> FF  $|A|^2$  is defined as the sum of the squares of the principal curvatures.

20

We define mean curvature flow and volume-preserving mean curvature flow.

#### Notation

- 5  $(M_t)$  is a family of evolving smooth 2D manifolds such that  $M = M_0$  is given.  
 $N(x, t)$  is the normal at  $x \in M_t$ .  
 $H(x, t)$  is the mean curvature evaluated at  $x \in M_t$ .  
 10  $h(t)$  is the average value of  $H(x, t)$  on  $M_t$ .

Mean curvature flow (mcf) is defined as the solution to the initial and boundary value problem

$$\frac{\partial M_t}{\partial t} = -H(x, t) \cdot N(x, t). \quad [4]$$

- 15 Volume-preserving mean curvature flow (vp-mcf) is defined as the solution to the initial and boundary value problem  $\frac{\partial M_t}{\partial t} = -(H(x, t) - h(t)) \cdot N(x, t)$ . [5]

Figure 6 illustrates that, except in ideal  
 20 circumstances (when the input is a smooth closed convex region or a graph), a surface evolves under mcf to a point. Technically, mcf develops a singularity in finite time. See, K. Museth, D. Breen, R. Whitaker, A. Barr, Level Set Surface Editing Operators, SIGGRAPH 2002.

- 25 A straightforward way to prevent annihilation of this shape is to stop the mcf after some number of time steps, inspect the results, and maybe resume the process. This is not convenient in a production environment. In fact, the manner in which uncontrolled mcf annihilates a  
 30 shape enables us to attach a recognition procedure that mcf can call to decide when to ask the human for permission to resume the figure's evolution.

Figures 7a-f forms a series of six images showing vpmcf suppressing noise. See, A. Kuprat, A. Khamayseh, D. George, L. Larkey, Volume Conserving for Piecewise Linear Curves, Surfaces, and Triple Lines, Journal of

5 Computational Physics, 172 (2001), pg. 98-118. In Figure 7a, the southern hemisphere is corrupted with a significant amount of Gaussian noise. By Figure 7c, it makes sense to consider how much additional noise, if any, must be removed before the smoothed result is an  
10 acceptable approximation.

We are interested in surfaces of revolution. The following result has been obtained regarding the behaviour of surfaces of rotation under vpmcf. See, M. Athanassenas, Volume-preserving mean curvature flow of  
15 rotationally symmetric surfaces, Comment. Math. Helv. 72(1997), pg. 52-66.

Theorem (Athanassenas)

20 Let  $M_0$  be a smooth rotationally symmetric surface enclosing a sub-volume  $V$ . Let  $S$  be a slab of thickness  $\tau > 0$  that is bounded by the  $z = 0$  and  $z = \tau$  height field planes. Suppose that  $M_0$  satisfies the following two conditions.

25

- a.  $M_0$  has a line of intersection in the  $z = 0$  and  $z = \tau$  height field planes.
- b. The end points of each line of intersection between  $M_0$  and  $S$  meet an end of  $M_0$  at a right  
30 angle.

If the volume of  $V$  is greater than  $\tau$  times the area of  $M$ , then  $M_t$  evolves under vpmcf to a cylinder.

, As an example of the condition on the lower bound on volume, consider the case of a right cylinder of height  $\tau$  and radius  $r$ . This cylinder has volume  $V$  equal to  $\pi r^2 \tau$ , while its surface area  $M$  is equal to  $2\pi r \tau$ . Hence the lower bound on the volume is satisfied exactly when  $\pi r^2 \tau \geq 2\pi r \tau^2$ , i.e.,  $r \geq 2\tau$ . Heuristically, the bound is satisfied for "squat" cylinders. We observe that a sphere cannot satisfy the volume to area relationship. To do so would imply that there exists  $r > 0$  such that  $\frac{4}{3}\pi r^3 / 4\pi r^2 = \frac{r}{3} \geq 2r$ .

Figure 8 illustrates the orthogonality condition of the theorem proposed by Athanassenas. In this diagram we show two vertical cross-sections. In the figure on the left the intersection of the figure with the top and bottom planes must satisfy the right angle hypothesis. The curvature flow takes care of the irregular vertical surfaces either end of the figure. In finite time  $vpmcf$  generates from the figure on the left the figure on the right.

Volume preservation is essential for earth model applications, so we prefer  $vpmcf$  to ordinary  $mcf$ . Later in the description, we will use this theorem to reduce the discrepancy between an idealized representation of shape and a sampled data surface.

Another important class of smooth surfaces are those that are star-shaped. A surface is star-shaped if there exists a point  $P$  on the surface such that a line segment  $PQ$  that is entirely contained in the surface can join every other point  $Q$  in the surface.

It has been shown that star-shaped closed smooth surfaces are stable under  $mcf$ . See, K. Smoczyk, Star-

shaped hypersurfaces and the mean curvature flow,

Manuscripta Math. 95 (1998), pg. 225-236.

We show now that vpmcf suppresses additive high frequency harmonics before decaying the underlying low frequency shape signal. Vpmcf enjoys the property that surface area is always decreasing in time.

$$\frac{d |M_t|}{dt} = - \int_M (H - h)^2 dg, \leq 0. \quad [6]$$

We frequently need to compute mean and Gaussian curvature for a single valued surface over a plane, i.e., a graph. Suppose that  $S = S(x,y)$ . Then the formulae for mean curvature  $H$  and Gaussian curvature  $K$  are as follows.

$$K = \frac{s_{xx}s_{yy} - s_{xy}^2}{(1 + s_x^2 + s_y^2)^2} \text{ and } H = \frac{1}{2} \frac{(1 + s_x^2)s_{yy} - 2s_x s_y s_{xy} + (1 + s_y^2)s_{xx}}{(\sqrt{1 + s_x^2 + s_y^2})^3} \quad [7]$$

We model a surface as a collection of patches, where each patch is taken from a surface of revolution, say  $S = (\phi(v) \cdot \cos u, \phi(v) \cdot \sin u, \psi(v))$ , such that  $v \in (a,b)$ ,  $u \in (0, 2\pi)$ , and  $\psi(v) \neq 0$ . The formulae for mean curvature  $H$  and Gaussian curvature  $K$  for a surface of revolution is as follows.

$$K = -\frac{\phi''}{\phi} \text{ and } H = \frac{1}{2} \frac{-\psi' + \phi(\psi'\phi'' - \psi''\phi')}{\phi} \quad [8]$$

For the proofs, see, M. do Carmo, *Differential Geometry of Curves and Surfaces*, Prentice Hall, 1976, pages 162-163.

We need to understand how mcf behaves when applied to a noisy surface  $S$ , where  $S$  is either single valued over a plane or is a surface of revolution. The above

formulae imply that if  $S$  is an entire graph, then the harmonic number  $N$  scales the mean curvature. Similarly, if  $S$  is a surface of revolution, then  $N^2$  scales the mean curvature. (Spherical harmonic polynomials have a cosine factor, so these estimates remain valid under the natural heat equation eigen-function expansion.) Consequently, the mean curvature integral involves a scale factor of either  $N^2$  or  $N^4$ . Therefore the rate of change of surface area becomes very negative as  $N$  increases. We conclude that vpmcf eliminates high frequency harmonics during the initial stages of the evolution ahead of low frequency harmonics that form the ideal shape. A maximum or minimum in the ideal shape will appear to move as vpmcf eliminates corrupting noise, but the critical point's location will stabilize as the noise disappears.

Importantly, when a critical point's location stabilizes, it does not move later in the evolution unless vpmcf begins to decay the shape. We remark that mcf can be turned off locally by resetting the mean curvature to zero.

We turn now to the question of how to decide when noise suppression turns into shape decay. Refer again to Figures 7a-f, which show the smoothing of a noisy sphere under vpmcf. Athanassenas's theorem does not apply, since the sphere fails the volume bound assumption. However, it still makes sense to apply Kuprat et al.'s vpmcf procedure to the shape. When we do this we get Figures 7c-f.

It is reasonable to say that noise suppression reduces Figures 7a-b to Figures 7c-d. It is harder to say if image noise suppression or shape decay accounts for the transformation to Figures 7e-f. Therefore, we want



vpmcf to proceed without manual intervention to eliminate noise but to seek guidance when the flow causes the underlying shape to decay. Here is a way to monitor the elimination of noise and detect decay of the critical  
5 points in an underlying shape that relies on vpmcf.

1. Given a characteristic length, we embed a series of conical shapes in the surface. The base of the cone is either the outermost 1D boundary of the surface  
10 or it is an inflection point curve surrounding the patch that contains the maximum or minimum.
2. We recognize minima and maxima in its 2D enclosure using a standard nested bounding box algorithm. If the surface is implicit, then we can localize the  
15 region by testing the implicit surface's triangulated parent.
3. Use this 2D enclosure as the top of the (noisy) cone. Note that we cannot assume that each maximum or minimum is topologically isolated, e.g., a ridge  
20 might exist.
4. Apply any mean curvature flow procedure, e.g., D3b, to the surface and monitor the effect on the cone's slant height. Mean curvature flow theory says that the slant height decreases as the noise is removed  
25 (it becomes straighter). However, when the mean curvature flow begins to destroy the intrinsic shape of the surface in the vicinity of the cone, then the slant height will decrease beyond a threshold. Therefore, the test for adequate smoothing is to  
30 compare the ratio of slant height before smoothing to the result obtained after each iteration.

Figure 9 is an aerial image of part of Big Bend National Park, showing the approximation of a plateau to  
35 a characteristic length scale cone. It is difficult to precisely locate the maxima on the plateau, but it is

easy to enclose the region containing the maxima in a tight loop. It is unimportant that the cone does not have a circular cross section.

Figure 10 is a side view of a noise cone structure.

5 When monitoring noise suppression on the surface of a geobody, e.g., it is useful to have a noise-monitoring device for thin undulating cross section. We replace a torus by a cone. We use the cone to monitor shear stretching and erosion of an interface. A clear instance  
10 of this phenomenon is Figure 7c.

According to the invention, mean curvature flow and framework I/O will now be discussed in further detail. Singularities mark an end to the smooth evolution of a  
15 shape under mcf. A singularity is frequently easier to identify on an image than is the interface that corresponds to the precise start of the flow. The flow imposes a natural partition of the framework. Each region in the partition is a self-contained expression of mcf.  
20 When we think about sending and receiving an update to a framework, we prefer to send and receive a mcf problem with boundary conditions rather than an opaque byte stream. We specify the solution form - whether the flow uniformly expands or contracts the solution or smoothes  
25 the initial data -and provide beginning and end surface data. We describe the intermediate surfaces by recording the time states that correspond to the intermediate surfaces. We also send critical point data for each intermediate surface. Interested applications run the  
30 vpmcf script and reconstruct the update locally. We trade fast CPU for less fast I/O.

Here are three illustrations of this idea. Figure 11 is a NASA satellite image of the Labrador Trough. In this image we notice that the sediment resembles a longitudinal cross section of a brain with an attached  
5 spinal cord. Singularities separate "brain tissue" from the stem of the "spinal cord". A singularity also subdivides the "cerebellum".

Figure 12 shows a sequence of folded sediment on the coast of the Gulf of Oman. We model this as a  
10 uniformly expanding (seen right to left) solution to mcf. Ecker proved that a uniformly expanding solution to mcf is given by the equation  $M_i = \sqrt{t} \cdot M_1$ , provided that the initial fold is approximately a cone.

Figure 13 is an image illustrating progressive  
15 flattening of an overburden covering a large salt intrusion. We notice that the fault block that occupies the left half of the image (indicated by the lower white arrow) displays a gradual flattening in space and time as the top of the salt's intrusion is progressively reduced  
20 as the sediment was deposited on top of the salt (indicated by the upper white arrow).

According to the invention, a preferred technique of 2D parameterization will now be discussed in further  
25 detail. Many surface editing operations are more efficient when the operator can access the surface's parameterisation. Height field data uses the (x,y) co-ordinate plane as the parameter space and coordinate projection as the parameter space mapping. We explain how  
30 to obtain a parameterisation of a smooth surface S with no assumptions regarding the orientation of the surface relative to the (x,y) co-ordinate plane.

We claim that there exists an invertible projection of  $S$  onto a cylinder that has 0, 1, or 2 end caps.

1. Given any two closed curves  $C_1$  and  $C_2$  on  $S$ . We partially order the two curves, say  $C_1 \leq C_2$ , if  
 5 there exists a 2D region  $R_2$  on  $S$  such that  $\partial R_2 = C_2$  and  $C_1 \subseteq R_2$ . We call the 2D region of  $S$  that is contained between  $C_2 \setminus C_1$  the collar that is bounded by  $C_2$  and  $C_1$ .

2. From the classification of smooth surfaces  
 10 in  $R^3$  we know that  $S$  has Euler Characteristic  $\chi(S)$  equal to 0, 1, or 2. The Euler Poincare Theorem says that  $\chi(S) = \#(\text{maxima}) + \#(\text{minima}) - \#(\text{saddle points})$ . Note that we use height as our Morse function, so the term "critical point" is a  
 15 contraction for "height field critical point".

3. We will prove our claim by induction on the number of saddle points on  $S$ .

4. Suppose that the number of saddle points on  $S$  is zero.

20 a. If  $\chi(S) = 2$ , then Reeb's Theorem says that  $S$  is diffeomorphic to a round sphere, which is diffeomorphic to a cylinder with two end caps.

b. If  $\chi(S) = 0$ , then  $S$  must be  
 25 diffeomorphic to a plane which is diffeomorphic to a cylinder with one end cap.

c. If  $\chi(S) = 1$  then  $S$  has either 1 maximum or 1 minimum but not both.

d. Construct a 1<sup>st</sup> order Taylor series  
 30 with center equal to the critical point and quadratic order error term.

e. Notice that the gradient term is trivial, since we expand about a minimum or maximum.

f. We apply a translation to the surface so that expansion point is the origin and has height equal to 0.

g. We conclude that after a suitable translation and  $(x,y)$  plane rotation a 2 term Taylor expansion about the critical point with a quadratic error estimator simplifies to a pure quadratic term.

h. Given  $\varepsilon > 0$ , we fit the Taylor expansion such that the error estimate is less than  $\varepsilon$ .

i. Then the Taylor series expansion within  $C_0$  is a cap/cup. We know that a cap/cup is diffeomorphic to a plane and that a plane is diffeomorphic to cylinder with one end cap. Furthermore, the open end of the cylinder has boundary  $C_0$ .

5. Suppose that the number of saddle points on  $S$  equals 1.

a. If  $\chi(S) = 2$ , then  $S$  possesses either (i) 2 maxima and 1 minimum or (ii) 2 minima and 1 maximum or (iii) 3 maxima or (iv) 3 minima.

b. Case (iii) is impossible, because Morse Theory says that a maximum contributes a 2D cell to the shape. If case (iii) were true, then

c. Case (iv) is impossible, because Morse Theory says that a minimum contributes a 0D cell to the shape. If case (iv) were true, then  $S$  contains no 2D cells.

Figure 14 is a diagram illustrating the Morse theoretical cell decomposition for a simple configuration of a capped and bent cylinder.

Morse Theory explains the cell decomposition of the shape. (See M. Hirsch, *Differential Topology*, Springer Verlag, 1976, pg. 156-164.)

5           d. This shape has a saddle point at location C.

          i. Morse Theory says that the surface contains a 1D cell that is attached to location C.

10          ii. We observe that this 1D cell is not a loop. Specifically, the point at location D is not part of the 1D cell.

15          e. This shape has a minimum at location D.

          i. Morse Theory says that the shape contains a 0D cell that is attached to location D.

20          f. This shape contains two maxima at locations A and B.

          i. Morse Theory says that the shape contains two 2D cells, and that each 2D cell is attached to a maximum.

25          ii. The boundary between the two 2D cells is the union of the 0D cell that is attached to location D and the 1D cell that is attached to location C.

30          iii. We decompose each 2D cell into the union of a Taylor series cap expanded about the maximum and a collar that is bounded by the loop suspended between locations C and D and the Taylor series circle of convergence.

35          g. Suppose that  $\chi(S) = 1$ . The Euler-Poincare formula says that the surface contains

either (i) 1 maximum and 1 minimum or (ii) 2 maxima or (iii) 2 minima.

i. An example configuration for case (i) is the upper half of a torus.

ii. An example configuration for case (ii) is a flat surface with two hills.

iii. An example configuration for case (iii) is a flat surface with two valleys.

h. Finally suppose that  $\chi(S) = 0$ . Then  $S$  contains either 1 minimum or 1 maximum, but not both. An example of this configuration is a single mountain or sinkhole attached to a plane.

6. We have specified the parametric mapping when  $S$  contains either 0 or 1 saddle point.

7. Now suppose that  $S$  contains  $N-1$  saddle points. Choose any saddle point and pass a height field plane through it, subdividing  $S$  in two. At least one of the two parts contains fewer saddle points than does  $S$ . Define  $S^*$  to be this part of  $S$ .

a. By induction we know that  $S^*$  is diffeomorphic to either a cylinder with a hole in its lateral surface, or a cylinder that has 0 or 1 end caps.

b. Closing the hole in  $S^*$  corresponds to either closing a hole in the walls of a cylinder or to attaching an end cap to the cylindrical surface that we created in  $xyz$  space.

Figures 15-17 show diagrams to aid in the understanding of the bulls eye construction. In Figure

16, we invertibly map the possibly patched  $A$  to the planar unfolding of its interior faceted cylinder. Figures 17a and 17b illustrates how to perform the bulls eye construction in the region of a saddle point. The saddle point is indicated with the dot 10 in Figures 17a and 17b. This process is preferably repeated for every saddle point of the shape.

According to the invention, tri-linear interpolation, implicit surfaces, and critical points will now be described in further detail. In particular we herein discuss the analysis of the tri-linear interpolation approximation to the signed distance function on a 3D structured grid. We derive necessary two conditions that the tri-linear interpolator must satisfy if the grid cell contains a height field critical point. One condition specifies a relationship between the tri-linear coefficients and the critical value. The other condition establishes a second relationship among four of the tri-linear coefficients. Taken together, we show that a height field critical point for an implicit surface must be embedded in the grid cell faces and can never be found in the interior of the grid cell unless the implicit surface is a plane.

Let  $G$  denote a 3D structured grid with typical grid cell  $C$ . We assume that an implicit surface  $S$  is contained in  $G$  and in particular that  $C \cap S \neq \emptyset$ . We denote the tri-linear interpolation function on  $C$  by  $\sigma$  and we assume that  $C$  is small enough that  $\sigma$  is a good approximation to the signed distance function that implicitly defined  $S$ .



We begin with the definition of tri-linear interpolation

$$\sigma(x, y, z) = A(x, y) + B(x, y) \cdot z \quad (1)$$

where

$$\begin{aligned} A(x, y) &= a_0 + a_1x + a_2y + a_3xy \\ B(x, y) &= b_0 + b_1x + b_2y + b_3xy. \end{aligned} \quad (2)$$

For later reference, we note that A and B are harmonic, i.e.,

$$\nabla^2 A = \nabla^2 B = 0 \quad (3)$$

We are interested in the zeroth level of  $\sigma$ . If  $\sigma = 0$ , then either  $B = 0$  or  $B \neq 0$ . We suppose that  $B \neq 0$ . Then

$$z = -\frac{A(x, y)}{B(x, y)}. \quad (4)$$

We know that height field critical points are found when

$$\frac{\partial z}{\partial x} = \frac{\partial z}{\partial y} = 0. \quad (5)$$

This condition is satisfied when

$$\begin{aligned} B \frac{\partial A}{\partial x} - A \frac{\partial B}{\partial x} &= 0 \\ B \frac{\partial A}{\partial y} - A \frac{\partial B}{\partial y} &= 0 \end{aligned} \quad (6)$$

Rewriting (6)

$$\frac{A}{B} = \frac{\frac{\partial A}{\partial x}}{\frac{\partial B}{\partial x}} = \frac{\frac{\partial A}{\partial y}}{\frac{\partial B}{\partial y}} \quad (7)$$

5 Using (7)

$$\begin{aligned} \frac{\partial}{\partial y} \left( B \frac{\partial A}{\partial x} - A \frac{\partial B}{\partial x} \right) &= \\ \left( \frac{\partial B}{\partial y} \cdot \frac{\partial A}{\partial x} - \frac{\partial B}{\partial x} \cdot \frac{\partial A}{\partial y} \right) + (B a_3 - A b_3) &= \quad (8) \\ (B a_3 - A b_3) &= 0. \end{aligned}$$

The Hessian matrix of 2<sup>nd</sup> partial derivatives  
10 evaluated at the critical point is

$$\begin{aligned} \frac{\partial^2 z}{\partial x^2} &= \frac{-2B \frac{\partial B}{\partial x} \left( B \frac{\partial A}{\partial x} - A \frac{\partial B}{\partial x} \right)}{B^4} = 0 \\ \frac{\partial^2 z}{\partial y^2} &= \frac{-2B \frac{\partial B}{\partial y} \left( B \frac{\partial A}{\partial y} - A \frac{\partial B}{\partial y} \right)}{B^4} = 0 \quad (9) \\ \frac{\partial^2 z}{\partial x \partial y} &= \frac{B \frac{\partial^2 A}{\partial x \partial y} - A \frac{\partial^2 B}{\partial x \partial y}}{B^4} = \frac{B a_3 - A b_3}{B^4} = 0. \end{aligned}$$

We conclude that the Hessian matrix of 2<sup>nd</sup> partial  
derivatives is identically zero. We are led to consider  
what kinds of shape have the property that in a local  
20 neighborhood of a critical point the matrix of second  
partial derivatives is identically zero.

We have enough information to compute the Gaussian  
curvature of  $z = z(x, y)$ . Recall that for a graph  $z =$   
 $z(x, y)$  that its Gaussian curvature  $K(x, y)$  is

$$K(x, y) = \frac{\frac{\partial^2 z}{\partial x^2} \cdot \frac{\partial^2 z}{\partial y^2} - \left(\frac{\partial^2 z}{\partial x \partial y}\right)^2}{\left(1 + \left(\frac{\partial z}{\partial x}\right)^2 + \left(\frac{\partial z}{\partial y}\right)^2\right)^2} \quad (10)$$

We notice that the signum of  $K(x, y)$  depends only on its numerator. Substituting (3) into the numerator of (9), we discover that the numerator of  $K(x, y)$  is

$$-\left(\frac{\partial z^2}{\partial x \partial y}\right)^2 = -(B \cdot a_3 - A \cdot b_3) + \left(\frac{\partial A}{\partial y} \cdot \frac{\partial B}{\partial x} + \frac{\partial A}{\partial x} \cdot \frac{\partial B}{\partial y}\right) \quad (11)$$

Hence the Gaussian curvature  $K(x, y) \leq 0$  everywhere.

As an illustration we consider the "monkey saddle"  $M(x, y)$ , which coincidentally is also a spherical harmonic polynomial  $M(x, y) = \text{Re}(Y_{33}) = x^3 - 3xy^2$ . The monkey saddle has a single critical point, which is the origin  $(0, 0)$ .

The matrix  $D$  of 2<sup>nd</sup> partial derivatives is

$$D = \begin{bmatrix} 6x & -6y \\ -6y & -6x \end{bmatrix}. \quad (12)$$

Substituting  $(x, y) = (0, 0)$ , we find that the 2<sup>nd</sup> partial derivatives matrix is identically 0. We conclude that the origin is a degenerate saddle point for  $M(x, y)$ .

Figure 18 shows two views of an example of a monkey saddle. In particular the monkey saddle is  $M(x, y)$  given by the equation above. The image on the left is shaded according to mean curvature, while the image on the right is shaded according to Gaussian curvature. We have placed a white dotted circle around the critical point.

The critical point is a degenerate saddle point. We see this by substituting the samples defined by the white circle and observing the pattern of  $+/-$  signs. As an example, let  $0 < a < b$ . Then  $((+/-)a, (+/-)b)$  produces the

pattern  $(-, -)$ ,  $(-, +)$ ,  $(-, -)$ , and  $(-, +)$  clockwise from Quadrant I.

The Gaussian curvature of the monkey saddle is (Gray, pages 382-383)

5

$$K(x, y) = -\frac{36(x^2 + y^2)}{(1 + 9x^4 + 18x^2y^2 + 9y^4)^2} \quad (13)$$

(See, A. Gray, *Modern Differential Geometry of Curves and Surfaces with Mathematica 2nd Edition*, CRC Press, 1998, pages 382-383).

10

Summarizing the analysis for  $B \neq 0$ , we have shown the following.

1. A grid cell contains at most one height field critical point.
2. If a grid cell does contain a critical point, then the critical point's coordinates are uniquely determined from the tri-linear interpolator's coefficients. We use this as a quick test for assessing the existence of a critical point in a grid cell.
3. The matrix of 2<sup>nd</sup> partial derivatives is identically zero when evaluated at the critical point.
4. The Gaussian curvature  $K(x, y) \leq 0$  and equals zero exactly at the critical point.
5.  $z = z(x, y)$  is harmonic, so by the Maximum Principle for harmonic functions on compact sets, we know that the minimum and maximum value for  $z$  on a grid cell will be found on the grid cell corners.

30

It has been remarked that the behavior of the tri-linear interpolation function is determined in the region

5 of a critical point by the behavior of  $\frac{\partial z}{\partial x}$ ,  $\frac{\partial z}{\partial y}$ , and  $\frac{\partial z}{\partial z}$ . See,

G. Weber, G. Scheuermann, H. Hagen, B. Hamann, Exploring Scalar Fields Using Critical Isovalues, <http://graphics.cs.ucdavis.edu/~hamann/WeberScheuermannHagenHamann2002.pdf> ("Weber"). We agree, which is Morse Theory

10 should be applied.

Weber shows that a tri-linear interpolation function can have a critical point on the edge of a grid cell if and only if the tri-linear interpolation function is constant along the edge. Weber does not assume that the

15 tri-linear interpolation approximates a signed distance function. Weber also obtains a simple test for the existence of a maximum at grid cell vertex  $(0,0,0)$  by looking at the value of the function at the tetrahedral corners  $(1,0,0)$ ,  $(0,1,0)$ , and  $(0,0,1)$ .

20 In our situation Weber's condition says that  $a_0 > \max(a_1, a_2, b_0)$  implies that  $(0,0,0)$  is a maximum of  $T(x,y,z) = A(x,y) + B(x,y)*z$ . We note that  $T(0,0,0) = a_0$  and that

$$\begin{aligned} \left. \frac{\partial T}{\partial x} \right|_{(0,0,0)} &= 0 \\ \left. \frac{\partial T}{\partial y} \right|_{(0,0,0)} &= 0 \\ \left. \frac{\partial T}{\partial z} \right|_{(0,0,0)} &= B(0,0) = b_0 \end{aligned} \quad (14)$$

25

Checking 2<sup>nd</sup> mixed partials

$$\frac{\partial^2 T}{\partial x^2} = \frac{\partial^2 A}{\partial x^2} + z \cdot \frac{\partial^2 B}{\partial x^2} = 0$$

$$\frac{\partial^2 T}{\partial y^2} = \frac{\partial^2 A}{\partial y^2} + z \cdot \frac{\partial^2 B}{\partial y^2} = 0$$

$$\frac{\partial^2 T}{\partial z^2} = 0$$

$$\frac{\partial^2 T}{\partial x \partial y} = \frac{\partial^2 A}{\partial x \partial y} + z \cdot \frac{\partial^2 B}{\partial x \partial y} = a_3$$

$$\frac{\partial^2 T}{\partial x \partial z} = \frac{\partial B}{\partial x} = b_1 + b_3 y \quad (15)$$

$$\frac{\partial^2 T}{\partial y \partial z} = \frac{\partial B}{\partial y} = b_2 + b_3 x$$

5

Therefore the first order Taylor series expansion of the tri-linear interpolation function about (0,0,0) inside a grid cell cube is given by the expression

$$\begin{aligned} T(x, y, z) &= a_0 + b_0 z + (b_1 + b_3 y)xz + (b_2 + b_3 x)yz \\ &= a_0 + b_0 z + b_1 xz + b_2 yz + b_3 xyz + b_3 xyz \quad (16) \\ &= a_0 + B(x, y)z + b_3 xyz \end{aligned}$$

10

This says that in a local neighborhood of (0,0,0) that the tri-linear interpolation function is a harmonic polynomial and therefore the Maximum Principle applies.

15

We conclude that on the tetrahedron formed by the four grid cell vertices that maximum occurs at the grid cell vertex  $a_0$  or  $b_0$ . We invoke Weber's assumption and conclude that the maximum occurs at  $a_0$ . It is not necessary to assume the other inequalities in Weber's assumption.

20

We consider now the case that  $\sigma = 0$  and  $B = 0$ . We begin by observing that  $\sigma = 0$  implies that  $B = 0$  if and only if  $A = 0$ . Therefore,

$$y = -\frac{a_0 + a_1x}{a_2 + a_3x} = -\frac{b_0 + b_1x}{b_2 + b_3x} \quad (17)$$

Again we look for solutions to the zero gradient equation.

5

$$\frac{dy}{dx} = -\frac{a_1a_2 - a_0a_3}{(a_2 + a_3x)^2} = 0 \text{ implies that } a_1a_2 - a_0a_3 = 0$$

and

(18)

$$\frac{dy}{dx} = -\frac{b_1b_2 - b_0b_3}{(b_2 + b_3x)^2} = 0 \text{ implies that } b_1b_2 - b_0b_3 = 0$$

Again we obtain a relationship among the tri-linear interpolator coefficients that must be satisfied in order that a grid cell face contain a critical point on a curve running through the grid cell face.

Suppose that a grid cell face contains a critical point of a curve. Again the second derivative  $\frac{d^2y}{dx^2} = 0$ , so we characterize the nature of the critical point by sampling the gradient on a tight neighborhood of the critical point.

We conclude that there exists at most 1 critical point on a curve running through a grid cell face and that the (x, y) coordinates of a critical point are uniquely determined in terms of the tri-linear interpolator's coefficients.

According to the invention shape index and shape identification techniques will now be described in further detail. According to a preferred embodiment, shape identification depends on a dimension - independent

measure of the principal curvatures at a point known as the Koenderink and van Doorn shape index  $si$ .

$$si = \frac{2}{\pi} \arctan \frac{\kappa_1 + \kappa_2}{\kappa_1 - \kappa_2} = \frac{2}{\pi} \arctan \frac{H}{\sqrt{H^2 - K}},$$

where  $\kappa_1 \geq \kappa_2$ .

- 5 Shown below is a chart of the shape index map's range  $[-1.0, +1.0]$ , which goes from most concave to most convex. We note that a shape index value of zero corresponds to a zero mean curvature surface, which for the case of a compact surface, equates to a catenoid or a
- 10 compact planar region.

Local shape	si interval	Local shape	si interval
spherical cup	$[-1, -7/8)$	saddle ridge	$[1/8, 3/8)$
trough	$[-7/8, -5/8)$	ridge	$[3/8, 5/8)$
rut	$[-5/8, -3/8)$	dome	$[5/8, 7/8)$
saddle rut	$[-3/8, -1/8)$	spherical cap	$[7/8, 1]$
saddle	$[-1/8, 1/8)$		

- Cantzler et al. have computed a correspondence between shape attributes defined by a Gaussian and mean
- 15 curvature value pair and the shape index map range. See, H. Cantzler, R. Fisher, Comparison of HK and SC curvature description methods, <http://www.dai.ed.ac.uk/homes/rbf/hc3dim.ps.gz>. See, the following tables.



	$K < 0$	$K = 0$	$K > 0$	Shape	Index range
$H < 0$	Saddle Valley (Sv Hy)	Concave Cylinder (-Cy)	Concave Ellipsoid (-El)	Concave Ellipsoid (-El)	$S \in [-1, -5/8)$
$H = 0$	Minimal (M Hy)	Plane (Pl)	Impossible	Concave Cylinder (-Cy)	$S \in [-5/8, -3/8)$
$H > 0$	Saddle Ridge (Sr Hy)	Convex Cylinder (+Cy)	Convex Ellipsoid (+El)	Hyperboloid (Hy)	$S \in [-3/8, 3/8)$
				Convex Cylinder (+Cy)	$S \in [3/8, 5/8)$
				Convex Ellipsoid (+El)	$S \in [5/8, 1]$

As an example, we compute the shape index of a torus.

5

a. The torus's parameterization is

$$((a+b \cdot \cos v) \cos u, (a+b \cdot \cos v) \sin u, b \cdot \sin v),$$

where we assume that  $a > b > 0$ .

b. The principal curvatures are  $k_1 = -\frac{\cos v}{a+b \cdot \cos v}$  and  $k_2 = -\frac{1}{b}$ .

10 c. Therefore  $\frac{k_1+k_2}{k_1-k_2} = -(1+\frac{2b}{a} \cos v)$ .

d. This quotient covers the range  $[-3.0, +1.0]$ ; hence the shape index covers the interval  $[-0.80, +0.50]$ , which corresponds to "trough" to "ridge".

15 Certain principal curvature pairs are distinguished.

1. If  $\kappa_2 = \kappa_1$ , then the shape index is  $\pm 1.0$ , as the  $\text{signum}(\kappa_2) = -/+1$ .

2. If  $0 = \kappa_2 > \kappa_1$ , then the shape index is  $-1/2$ .

20 3. If  $\kappa_2 > \kappa_1 = 0$ , then the shape index is  $1/2$ .

4. If  $\kappa_2 = -\kappa_1$ , then the shape index is 0.

5. The shape index of a maximum is 1.0.

6. The shape index of a minimum is -1.0.

7. If the shape index is discretized in increments of size  $\Delta s$ , then the principal curvatures will

25

be discretized according to the following formulae

Shape index expresses a relationship between  
5 principal curvatures. For example, we expect the shape index in the region of an inflection point is approximately 1/8. Plugging into the shape index definition, we discover that

$$10 \quad \kappa_2 = \kappa_1 \cdot \left( \frac{\tan\left(\frac{\pi}{2} \cdot \frac{1}{8}\right) - 1}{\tan\left(\frac{\pi}{2} \cdot \frac{1}{8}\right) + 1} \right) = -0.99023 \cdot \kappa_1.$$

The shape index enables a human to express a threshold change in curvature in a dimension-independent manner. This correspondence is fundamental to the  
15 robustness of our shape identification scheme. Measurements are always tainted with noise. Therefore it preferable to identify intervals rather than point values for attribute correspondence.

### *Definitions*

Let  $A, B \in S$  and let  $s_A, s_B$  be the shape index at  $A, B$ .

20 By definition  $\tan\left(\frac{\pi}{2} \cdot s^A\right) = \theta^A$  and  $\tan\left(\frac{\pi}{2} \cdot s^B\right) = \theta^B$ , where

$$\theta^A = \frac{\kappa_1^A + \kappa_2^A}{\kappa_1^A - \kappa_2^A}, \text{ where } \kappa_1^A \text{ and } \kappa_2^A \text{ are principal curvatures at } A.$$

Likewise for  $\theta^B$ .

$$\text{Thus } \tan\left(\frac{\pi}{2} \cdot (s^B - s^A)\right) = \frac{\theta^B - \theta^A}{1 - \theta^B \cdot \theta^A} \text{ or } (s^B - s^A) = \frac{2}{\pi} \arctan\left(\frac{\theta^B - \theta^A}{1 - \theta^B \cdot \theta^A}\right)$$

This formula relates the shape index principal curvature quotient in shape index increments. For example

$$\text{if } (s^B - s^A) = \frac{1}{8}, \text{ then } \tan\left(\frac{\pi}{16}\right) = 0.0034 = \frac{\theta^B - \theta^A}{1 - \theta^B \cdot \theta^A}.$$

Holding  $\theta^A$  fixed, then  $\tan\left(\frac{\pi}{16}\right) \cdot (1 - \theta^B \theta^A) = \theta^B - \theta^A$  implies that

$$\theta^B = \frac{\tan\left(\frac{\pi}{16}\right) + \theta^A}{1 + \tan\left(\frac{\pi}{16}\right) \cdot \theta^A} = \frac{0.0034 + \theta^A}{1 + 0.0034 \cdot \theta^A}.$$

Now we can utilize the formula relating the value of a shape index to the ratio of the constituent principal curvature.

10

According to a preferred embodiment of the invention, techniques for curvature-adaptive sampling of a smooth surface will now be described in further detail.

15

Due to popularity of 2D FFT methods, it is common practice to sample a surface based on a fixed spatial step size. For smooth data, we know that a low order Taylor polynomial expansion can supply sample data to whatever a priori precision and at whatever spacing is acceptable. There is no need to store a large array when an algebraic expression can be evaluated on demand. Our method for curvature-based sampling is straightforward.

20

1. We are given a cloud of points. Using Hoppe's tangent plane fitting procedure (Hoppe, pages 22-25), we loop through the input point cloud fitting tangent planes.

25

2. At each tangent plane, we determine if the parent point is a height field critical point. We record the set of all critical points  $\{C_k\}$ . We use the symbol  $T(C_k)$  to denote the tangent plane at  $C_k$ .
3. At each critical point  $C_k$ , we define a neighborhood  $N(C_k)$  about  $C_k$  in the point cloud such that the tangent plane  $T(C_k)$  is a parameterization of the triangulation of the points in  $N(C_k)$ . Abusing notation slightly, we use  $N(C_k)$  to denote the triangulation of the point cloud.
4. Using equations (4.7<sub>1</sub>) and (4.7<sub>2</sub>) we estimate both principal curvatures and the associated shape index on  $N(C_k)$ .
5. Given a shape index increment, we apply the analysis developed in Section 8 to partition  $N(C_k)$  into shape index equivalence classes. We chose to seed the shape index equivalence classes with critical points so that there is the least ambiguity in the shape index assignment.
6. If the critical point neighborhoods do not cover completely the implicit surface, then search the remaining surface for regular points that have an unambiguous shape index interval assignment.
7. Bin the remaining unassigned sample points to new shape index equivalence classes.
8. Assign each shape index equivalence class to a distinct grid cell.

9. Done.

This algorithm uses just curvature information, since we apply it to the unorganized input point cloud.

5 We can improve the  $N(C_k)$  partition if we know a priori that the shape identification procedure described above has been applied. Using the information generated during shape identification, we construct a low order Taylor polynomial expansion that equals as a point set a shape index equivalence class. We begin with an estimate of the error that we expect if we expand the signed distance function (sdf) in a 1<sup>st</sup> order gradient Taylor expansion plus quadratic remainder term. Let  $s(x, y)$  represent the sdf over an open neighborhood  $N(x_0, y_0)$  in the  $(x, y)$  plane.

15 Then the Taylor expansion for  $s$  in  $N(x_0, y_0)$  is

$$s(x, y) = s(x_0, y_0) + \left[ \frac{\partial s}{\partial x}(x_0, y_0) \cdot (x - x_0) + \frac{\partial s}{\partial y}(x_0, y_0) \cdot (y - y_0) \right] + \frac{1}{2!} \left[ \frac{\partial^2 s}{\partial x^2}(\alpha x, \alpha y) \cdot (x - x_0)^2 + \frac{\partial^2 s}{\partial x \partial y}(\alpha x, \alpha y) \cdot [(x - x_0)(y - y_0)] + \frac{\partial^2 s}{\partial y^2}(\alpha x, \alpha y) \cdot (y - y_0)^2 \right]; \alpha = \alpha(x, y) \text{ and } 0 < \alpha < 1.$$

We translate  $s$  in the  $z$ -direction so that  $s(x_0, y_0) = 0$ , eliminating the constant term. Now rotate the orthonormal basis defined by the tangent plane of the sdf at  $(x_0, y_0)$  plus the  $z$ -axis so that it coincides with the orthonormal basis formed the canonical co-ordinate system.

25

Notes:

a. Rotation in the (x,y) coordinate plane will align any pair of orthogonal vectors the coordinate plane axes.

b. Rotating the surface so that  $s(x_0, y_0)$  is a maximum causes  $\nabla s(x_0, y_0) = 0$ .

Combining the translation and the rotation, the Taylor expansion is

$$s(x, y) = \frac{1}{2!} \left[ \frac{\partial^2 s}{\partial x^2}(\alpha x, \alpha y) \cdot x^2 + \frac{\partial^2 s}{\partial y^2}(\alpha x, \alpha y) \cdot y^2 \right]; \quad 0 < \alpha < 1.$$

The coefficients inside the square brackets are the principal curvatures at  $(\alpha x, \alpha y)$ . They can be computed from the mean and Gaussian curvature at  $(\alpha x, \alpha y)$ .

$$H(\alpha x, \alpha y) = \frac{1}{2!} \left[ \frac{\partial^2 s}{\partial x^2}(\alpha x, \alpha y) + \frac{\partial^2 s}{\partial y^2}(\alpha x, \alpha y) \right]$$

$$K(\alpha x, \alpha y) = \frac{\partial^2 s}{\partial x^2}(\alpha x, \alpha y) \cdot \frac{\partial^2 s}{\partial y^2}(\alpha x, \alpha y)$$

Using shape analysis, the true value of every term in the Taylor expansion is known. The Taylor disk records the first two terms in the expansion, the expansion point, the disk's radius of convergence, and the maximum error incurred on the convergence disk when a sample coordinate is approximated by just the constant and linear gradient terms. When an intersection curve is established, then the definition of the curve is attached. There is a separate attachment for every intersection curve.

The  $\alpha$  parameter is interesting. Given the center of the Taylor disk, the disk radius, and polar angle increments then the  $\alpha$  parameter describes the intersection as well as the principal curvatures along the intersection curve. (A more descriptive name for this parameter is "wireframe".) This parameter determines the adequacy of the interpolating function in the 3D grid. In other words, the adequacy depends on the curvature of the parent surfaces along the intersection path.

We prepare the topological analysis of a shape-based surface by creating a manifold whose charts are point sets that correspond to shape index intervals. We call this a shape index manifold. We explained above how to construct the manifold's charts and how to estimate the differential properties of a chart. These tasks make sense with no external context, i.e., a background framework. We refer to properties that make sense in this self-contained context as "intrinsic". Any property of a manifold that is not intrinsic is "extrinsic". An example of an extrinsic attribute is the relationship between the boundaries of a surface and the boundaries of a shape index manifold.

An intrinsic boundary is one that remains a boundary under rigid motion. It is a Cartesian tensor by virtue of this definition. This boundary separates regions that are well approximated by patches taken from a surface of revolution. An extrinsic boundary is a boundary that owes its existence to the configuration of background surfaces. Should the background surfaces move then the shape of the intersection and indeed the very existence of the intersection can change. The choice of solver depends on the dataset assumptions. The Shapes @ library

does not provide recognition or interaction services pertaining to intrinsic boundaries. We agree that a characteristic of a sound approach to point set classification is a robust algorithm to compute the intersection of two extrinsic boundaries. But we go one step further and say that intersection in a region that is devoid of extrinsic structure can be still be quite complicated, if the intersection involves a non-empty subset of a non-differentiable interface that separates two shapes.

We seek a data structure that conveys a framework overview. We want it to contain the complete boundary representation for the framework plus a synopsis of the shape of every framework surface and curve. We envision using this data structure to reply to browser level framework data base queries when the caller does not want to open the framework with the standard geometry services toolkit.

We define a structural synopsis to be a Shapes/GOI topology graph (also known as a boundary-representation or "b-rep") plus a shape index manifold description of every 2D node in the b-rep.

Preferably, a Reeb graph is used to describe a configuration's Morse critical points and homotopic skeleton. See, M. Hilaga, Y. Shinagawa, T. Komura, T. Kunii, Topology matching for full automatic similarity estimation of 3D, SIGGRAPH 2001, pg. 203-212, and Silvia Biasotti, Topological techniques for shape understanding, <http://www.cg.tuwien.ac.at/studentwork/CESCG-2001/SBiasotti/>. We recall the definition of a Reeb graph. Let  $M$  be a path-connected manifold and let  $f$  be a real-valued on  $M$ . Then the Reeb graph associated with  $(M,$



$f$ ) is a set of  $(M, f), R$ ) equivalence classes that is defined by the relation  $(x, f(x)) \sim (y, f(y))$  if and only if  $f(x) = f(y)$  and  $x, y$  are members of  $f^{-1}(f(x))$ . In

practice, the nodes and arcs in a Reeb graph are

5 determined from continuous sampling of homotopic identification of height field contours. Since the height field is a Morse function, we obtain information regarding each non-degenerate critical point and the cell to which the critical point is attached. The discussion  
10 of 2D parameterization herein summarizes the relevant facts from Morse Theory.

Figure 19a shows the Reeb graph of a standard torus. Figure 19b schematically illustrates a 2D cell suspension that is induced from the axes and planes of symmetry and  
15 critical point theory. The Reeb graph's nodes in this case are critical points on the torus, since the critical points are isolated and non-degenerate. The graph contains 4 nodes. The bottom and top nodes correspond to the height field minimum and maximum. These two points  
20 lie on an isoparametric curve of constant positive Gaussian curvature. The other two nodes correspond to the lower and upper saddle points. They too lie on an isoparametric curve, but this curve has constant negative Gaussian curvature. It is easy to see that the symmetry  
25 group of the torus leaves invariant the orbit of a saddle point as well as the orbit of the min/max. We remark that observing this invariant behavior is an easy way to discover symmetry transformations.

A Reeb graph describes homotopic equivalence. Reeb's  
30 representation has no concept of shape. The Reeb graph says nothing about Gaussian curvature or mean curvature or shape index. There is no mention of the two opposing

curves of zero Gaussian curvature. Nor is there a description of the shape of the saddle point curve that bounds the interior void. Homotopic equivalence does not leave invariant 2D regions of constant shape index, so it is not possible to reason about symmetry orbits under Reeb equivalence.

Neither the Hilaga nor Biasotti references augment the Reeb graph substrate with curvature information, citing the natural instability of curvature estimation in noise. We agree that curvature estimation in a noisy environment is difficult, but we have above that it makes sense to treat a noisy surface as a smooth substrate that is contaminated with noise. We think of the representation of a noisy surface as a minimization problem in Lagrangian mechanics. The smooth approximant represents the kinetic energy in the decomposition. We define the curvature of the original surface to be that of the smoothed component of the original surface. The Riemann integral of the discrepancy between the smooth approximant and the original surface is a measure of the potential energy in the original surface. Noise introduces uncertainty into the curvature estimate. We compensate for this uncertainty by working with shape index intervals, rather than a point-specific value. We define a shape synopsis diagram (SSD) to a Shapes/GQI boundary representation where a 2D node is a shape index manifold.

We comment further that Hilaga reports the development of a similarity metric for a pair of triangulated surfaces  $S_1$  and  $S_2$ . Their idea is to create a level of detail hierarchy for each surface. The authors summarize each level of detail by constructing a Reeb

graph of the coarsened surface. Hilaga chooses the Reeb function to be the integral of geodesic distance measured at every vertex of  $S_1$  and  $S_2$ . Hilaga approximates the integral using Dijkstra's Algorithm. Hilaga argues that  
5 this Reeb function is superior to a height field because the integral is insensitive to orientation.

We want to compare Hilaga's method to the method of the present invention. This is not easy. Hilaga works with triangulated surfaces rather than implicit surfaces.

10 Consequently we must be careful regarding the meaning of the term "geodesic path". On a smooth surface we can define a geodesic curve to be the straightest possible path or the shortest possible path, since the two characterizations coincide. On a triangulated surface  
15 they do not. As is common practice, we select "straightest possible" geodesics because an existence proof is available for "straightest possible" whereas none exists if instead we opt for "shortest possible" geodesics.

20 We restrict attention to a single surface of revolution  $S$ , because there exists a theorem that says that a parallel on  $S$  is a geodesic exactly when the tangent vector at any point on the surface is parallel to  $S$ 's axis of symmetry. The symmetry group of  $S$  honors this  
25 constraint, so the geodesic is an orbit under the action of the symmetry group.

Figure 20 is cross section of the torus shown in Figure 19a. Figure 20 shows the torus opened along a planar surface that joins the saddle point circular orbit  
30 and the min/max circular orbit.

In Figure 20, we have overlaid the symmetry group orbits associated with critical points. We measure

criticality against the standard height field Morse function, because geological data is naturally observed in depth. We free ourselves of orientation and pose limitations by working with the symmetry group orbits of critical points rather than the isolated critical points themselves.

Figure 21 is a schematic of the shape synopsis diagram (SSD) of the torus shown in Figure 19a. The SSD reports locations in normal position coordinates and uses a homogeneous transformation to correctly position this data in model space. We also note that an SSD takes little storage beyond that already needed to instantiate the b-rep. We have placed details of the shape index manifold and shape index chart provided below.

Since an SSD augments the standard b-rep we attach a spatial frame to the b-rep node to reference the SSD. Since the top-level node in the SSD contains a database identifier, standard navigation methods can be used to locate the b-rep given the SSD. We call attention to the arrow notation in the SSD. We use an arrow to define the correspondence of 1D chart boundaries to 2D charts. The arrow that is attached to the concave chart signifies that the chart does not bound a sub-volume along its outside. Similar remarks pertain to the convex chart.

The Reeb graph of a cyclide is identical to the Reeb graph of a torus, as expected since the standard Reeb graph does not consider shape. The difference between a cyclide SSD and a torus SSD is the absence of circular orbits connecting critical points. That is, all of the height field critical points for a cyclide are isolated and are fixed by the cyclide's back to front reflection operator.

Figure 22 is a cyclide that is shaded according to Gaussian and mean curvature.

Next we construct the SSD for a 2-torus. Figure 23a is a bi-torus with its associated REEB diagram. Figure 23b is the visual representation of the bi-torus shape synopsis diagram. A shape index manifold is a patchwork, with each patch taken from a surface of revolution. So it makes sense to display the surfaces of revolution, where each surface is decorated with the bounding curves that define the patch selection. On the bi-torus's SSD there are two thin circular arcs plus the outer circle identify the two toroidal components in the bi-torus. We attached the "slab" label to the connective material between the two tori, because we perceive the top of the bi-torus to be flat, i.e., its Gaussian curvature is zero. The slab's internal boundary joins the upper and lower parabolic curves on both tori. We have suppressed the 1D orbits and critical point assignments to keep the diagram readable. The bi-torus is a genus 2 sphere, so there is 1 minimum and 1 maximum. Since the tori are tilted, the height field does not see the any critical points along either saddle point orbit. Finally, the interior surfaces of the slab are concave (hyperbolic) in order to conform to the torus's exterior convex surface.

The differences between an SSD and a Reeb graph are very clear. The use of homotopic identification means that the Reeb graph cannot distinguish homotopic figures that have significantly different curvature, e.g., a convex figure from a concave figure. Therefore shape index analysis is meaningless in the context of a Reeb graph.

We conclude that although we can map a Reeb graph into an SSD, a Reeb graph cannot support a shape

index manifold.

According to a preferred embodiment of the invention, an efficient hierarchical surface representation will now be described. We represent an implicit surface's signed distance function in a narrow band octree encoding of a regularly spaced Cartesian grid. We discuss herein how curvature and shape analysis of the implicit surface simplify the octree as a data structure. Smoothing or editing in general is likely to change a prior shape analysis, so we will also describe herein an adjunct shape index representation that enables fast updating of the octree's information archive.

1. We begin by computing the shape index on the implicit surface at the finest resolution in the octree.
2. We partition the shape index data into equivalence classes.
  - a. We find the finest resolution octants that contain the surface's height field critical points.
  - b. We define the following shape index relation on the octant corners that were located in the previous step.
  - c. We say that two octant corners are related when that their respective shape index values are contained in the same Cantzler sub division of the fundamental space  $[-1.0, +1.0]$  and that both values are bounded away from both ends of the Cantzler subdivision.
  - d. We make a second pass over every equivalence class of octree nodes that contains less than a

threshold number of samples. Let  $v$  be such a node and suppose that  $v$  is on the frontier of shape index equivalence classes  $\chi_1$  and  $\chi_2$ .

5 e. If  $\chi_1$  and  $\chi_2$  are approximated by a single elementary shape instance, then we will assign the node  $v$  to either  $\chi_1$  or  $\chi_2$ .

f. If  $\chi_1$  and  $\chi_2$  are not approximated by a single elementary shape instance, then we assign  $v$  to  $\chi_j$  if the error in the elementary shape  
10 approximation is less than a threshold

3. We introduce the shape index information to the coarser levels of the octree.

15 a. We say that a low-resolution octant is stable if there exists an elementary shape representation for all highest resolution level nodes that are controlled by the coarse level octant.

20 b. We record stability status. If a low-resolution node is stable, then it will use the elementary shape's algebraic evaluators for signed distance, mean and Gaussian curvature, etc.

c. We recognize that a stable low-resolution octree node  $v$  has the same shape resolution as  
25  $v$ 's finest resolution level components. If we want a truly coarser approximation, then we develop a separate family of elementary shapes for each resolution level in the octree.

30 4. We prune the stable regions of the octree.

- a. Given an octant  $Q$  at level  $L$  such that its leaf level resolution is part of an ideal elementary shape.
- b. We set a status bit in  $Q$  that says it coarsely resolves part of an ideal shape.
- c. Prune the branch of the octree rooted at  $Q$
- d. If  $Q$  does not coarsely resolve part of an ideal, then we keep the branch rooted at  $Q$ . Furthermore, we may need to use the leaf-level interpolator to estimate curvature.

The situation most favorable to this algorithm is when the root surface  $S^*$  contains a large stable region. This can happen if the leaf-level surface  $S$  contains a large region of zero Gaussian curvature, in which case the shape index for the region is  $\frac{1}{2}$  or  $-\frac{1}{2}$ . Another favorable situation is that both the mean curvature and Gaussian curvature are constant, e.g., a sphere, so that the shape index is again a constant.

Figure 24 is a diagram of the octree with a coarse level and leaf level shape index relationship indicated. Consistent texture-coding between corresponding regions indicates a stable shape index region.

We consider two examples. The Figure 25 is a diagram shows part of the French model. A single octree leaf defines each plateau. The hemispherical depression has constant mean curvature and constant Gaussian curvature, so in both regions only one octree leaf is needed.

Figure 26 is an image of the topography of Crater Lake, Oregon. Figure 26 shows two large plateaus in the Southwest part of the lake basin. There are large flat regions of the lakebed, so this algorithm will represent these regions economically. The small elevation bumps on the lakebed will be enclosed in extruded cylinders.



We anticipate that the algorithm will perform well on the large trimmed conical plateau in the rear.

According to a preferred embodiment of the invention, an implicit surface shape identification technique will be described. In particular we show how to uniformly approximate an implicit surface by a patchwork of smooth shapes, where each shape is a section of a surface of revolution. The implicit surface is not required to be smooth. We say that the volume between the given implicit surface and the patchwork of smooth shapes measures the misfit of the approximation. We improve the uniform approximation by reducing the misfit. We reduce the misfit by approximating the volume as a Riemann sum of generalized prisms.

Shape identification provides a much higher density of information. Figure 27 shows a salt weld in the Gulf of Mexico. See, M. Hodgkins, M. O'Brien, Salt sill deformation and its implications for subsalt exploration, The Leading Edge, August 1994, pg. 849-851. We enumerate the shapes that collectively represent this complicated geobody.

The shape legend for this image is as follows.

1	Paraboloid cap	6	Toroidal sector
2	Cylinder	7	Barrel
3	Toroidal sector	8	Conical sector
4	Barrel	9	Toroidal sector
5	Conical sector	10	Cone

Now we specify the shape identification algorithm.

#### Notation

S A noisy implicit surface.

- $S^*$  A smoothed version of  $S$ .  
 $G$  A 3D regularly spaced grid  
 $C$  A grid cell in  $G$  with corners  $\{c_0 \dots c_7\}$ .  
 $\sigma$  The signed distance function defined on  $C$  such  
 5  $\sigma^{-1}(0) = S \cap C \neq \emptyset$ .  
 $\tau$  Tri-linear interpolation associated with grid  
 cell  $C$  that approximates the signed distance  
 function  $\sigma$  on  $C$ .  
 $\sigma^*$  The symmetry group of  $\sigma$ .

10

Shape identification algorithm

1. We are given a 3D rectangular or rectilinear grid  $G$   
 that contains an implicit surface  $S$ .
- 15 2. Construct a smooth surface  $S^*$  from  $S$ , eliminating  
 noise, but not low frequency intrinsic shape.
3. Sample  $S^*$  such that there exists a sample at each  
 entry and exit point on each grid cell face in  $G$ .  
 We know how to do this, since we know the nature of  
 20 a smooth shape that tri-linear interpolation can  
 represent.
4. For each  $S^*$  sample point estimate the mean and  
 Gaussian curvature.
5. Compute the shape index at every  $S^*$  sample point.
- 25 6. Mark those samples that are close to the center of  
 a Cantzler shape index interval.
7. Mark those grid cell samples that are height field  
 critical points, i.e., minima, maxima, and saddle  
 points. (We know that these occur at grid cell  
 30 corners only.)

We identify shapes on  $S^*$ .

8. For each  $S^*$  critical point select grid cells  
 35 attached to the critical point that have consistent  
 mean curvature, Gaussian curvature, and shape index

estimators at all sample points in the grid cell  
These grid cell sets define the initial equivalence  
classes.

- 5           9. We want to define a shape from the region of  $S^*$   
inside the grid cell equivalence class. We check  
that each admitted grid cell's tri-linear  
interpolant has the same symmetry group. If there  
is no common symmetry group, then we subdivide the  
equivalence class into subclasses that do have a  
10          shared symmetry group.
10. Using the shape index data and the symmetry group,  
identify a surface of revolution that best fits the  
curvature and unit normal vector field data.

15          Let  $C$  be a grid cell that is unassigned to a grid  
cell equivalence class, but is adjacent to a grid cell  
that has been assigned to a grid cell equivalence class.  
We want a condition to test for admission to the  
equivalence class.

- 20          11. There are two categories of grid cells in an  
equivalence class. A member grid cell is either  
"shapely" or is a "misfit".
- 25          12. In order for the candidate grid cell to be admitted  
as "shapely", it must satisfy the following  
conditions.
- a. Its tri-linear interpolation function has the  
            same symmetry group as all other shapely grid  
            cell members.
- 30          b. If a shapely grid cell in the equivalence class  
shares a grid cell face with the candidate grid  
cell, then they share a smooth boundary across  
the grid cell face.
- 35          c. We re-compute the shape parameter vector and  
re-test all grid cells in the equivalence  
class. No "misfit" grid cell is allowed to

exceed the misfit tolerance and no shapely grid cell can become a misfit.

13. Test if the candidate grid cell is shapely.

14. If not, then test if the candidate can be considered a "misfit".

a. A misfit must be less than some threshold and no point on the surface sample in the candidate grid cell can be further from the ideal shape than some other threshold.

15. If the misfit is acceptably small, then we mark the grid cell as a "misfit" and admit the grid cell.

We specify a misfit reduction algorithm later in this part of the description.

It may be that some grid cells have not been assigned to an equivalence class. These grid cells are not associated with a shape that has a critical point in the smoothed implicit surface  $S^*$ .

16. Form a new equivalence class by finding connected sets of grid cells where the individual grid cell tri-linear interpolation functions have the same symmetry group and whose shape index samples lie in the same Cantzler shape index interval.

It may be that some grid cells can be assigned to more than one equivalence class. If we have a choice, then we assign the candidate to the class that accepts the candidate as shapely.

It may be that some grid cells have not been unassigned to an existing equivalence class. Since  $S^*$  is smooth, we know that noise is not a contributing factor.